Enhanced Orange II Removal Using Fe/Mn/Mg2-LDH Activated Peroxymonosulfate: Synergistic Radical Oxidation and Adsorption

Yajie Wang, Cui Qiu, Peng Cheng, Yuqing Li, Yunlong Ma, Xiuzhen Tao, Bo Weng, Gilles Mailhot

catalysts

MDPI

Article

Enhanced Orange II Removal Using Fe/Mn/Mg_2-LDH Activated Peroxymonosulfate: Synergistic Radical Oxidation and Adsorption

Yajie Wang [1], Cui Qiu [1], Peng Cheng [2,3,*], Yuqing Li [1], Yunlong Ma [1], Xiuzhen Tao [1], Bo Weng [4,5,*] and Gilles Mailhot [2]

1 School of Eco-Environmental Engineering, Guizhou Minzu University, Guiyang 550025, China; yajiewang@gzmu.edu.cn (Y.W.); qiucui@gzmu.edu.cn (C.Q.); liyuqing@gzmu.edu.cn (Y.L.); mayunlong@gzmu.edu.cn (Y.M.); Taoxiuzhen@gzmu.edu.cn (X.T.)
2 Institut de Chimie de Clermont Ferrand (ICCF) UMR 6296, Université Clermont Auvergne, CNRS, Clermont Auvergne INP, BP 80026, F-63171 Clermont-Ferrand, France; gilles.mailhot@uca.fr
3 Hubei Key Lab of Biomass Resource Chemistry and Environmental Biotechnology, School of Resources and Environmental Science, Wuhan University, Wuhan 430079, China
4 CAS Key Laboratory of Urban Pollutant Conversion, Institute of Urban Environment, Chinese Academy of Sciences, 1799 Jimei Road, Xiamen 361021, China
5 University of Chinese Academy of Sciences, 19A Yuquan Road, Beijing 100049, China
* Correspondence: peng.cheng@uca.fr (P.C.); bweng@iue.ac.cn (B.W.)

Abstract: In this study, Fe/Mn/Mg_2-LDH was utilized for the first time as a catalyst for peroxymonosulfate (PMS) activation to facilitate the removal of Orange II. This composite was characterized using various techniques, such as XRD, FTIR, SEM-EDS, BET, and XPS. The results revealed a well-defined lamellar structure of Fe/Mn/Mg_2-LDH with a metal molar ratio of Fe/Mn/Mg at 1:1:2. Moreover, the structural stability of Fe/Mn/Mg_2-LDH was confirmed through the XRD, FTIR, and SEM. Fe/Mn/Mg_2-LDH exhibited a good adsorption capacity towards Orange II and highly efficient PMS activation. The optimal removal efficiency of Orange II (98%) was achieved under the conditions of pH 7.0, [PMS] = 1.0 mmol L^{-1}, [Fe/Mn/Mg_2-LDH] = 1.6 g L^{-1}, and [Orange II] = 50 μM. Additionally, this system demonstrated good adaptability across a wide pH range. The presence of Cl^- and humic acids (HA) did not significantly inhibit Orange II removal, whereas inhibitory effects were observed in the presence of CO_3^{2-} and PO_4^{3-}. The removal mechanism of Orange II was attributed to a synergy of adsorption and oxidation processes, wherein the generated surface radicals ($SO_4^{\bullet-}{}_{ads}$ and $HO^{\bullet}{}_{ads}$) on the surface of the Fe/Mn/Mg_2-LDH played a predominant role. Furthermore, the Fe/Mn/Mg_2-LDH exhibited good reusability, maintaining a removal rate of 90% over five cycles of recycling. The Fe/Mn/Mg_2-LDH/PMS system shows promising potential for the treatment of wastewater contaminated with refractory organic pollutants.

Keywords: Fe/Mn/Mg_2-LDH; PMS activation; adsorption; Orange II; surface radicals

Citation: Wang, Y.; Qiu, C.; Cheng, P.; Li, Y.; Ma, Y.; Tao, X.; Weng, B.; Mailhot, G. Enhanced Orange II Removal Using Fe/Mn/Mg_2-LDH Activated Peroxymonosulfate: Synergistic Radical Oxidation and Adsorption. *Catalysts* **2024**, *14*, 380. https://doi.org/10.3390/catal14060380

Academic Editor: Aurora Santos

Received: 6 May 2024
Revised: 6 June 2024
Accepted: 10 June 2024
Published: 14 June 2024

1. Introduction

Recently, sulfate radical-based advanced oxidation processes (SR-AOP) have received attention due to their high efficiency in eliminating refractory organic pollutants in wastewater and soil [1,2]. The sulfate radical ($SO_4^{\bullet-}$) is characterized by its high redox potential (2.5–3.1 eV), long lifetime (30–40 μs) [3], and high reactivity with electron-rich organic pollutants [4]. $SO_4^{\bullet-}$ can be generated through the activation of persulfate (PS) or peroxymonosulfate (PMS). In the case of PMS, various methods such as ultraviolet (UV) light, heat, ultrasound, base granular activated carbon, and transition metals (Fe, Mn, Cu, Co, etc.) can be employed for its activation [5–7]. Notably, transition metal ions (TMI) activated PMS are favored for their cost-effectiveness and high efficiency [8]. However, the use of homogeneous systems faces limitations. For instance, Cobalt ions (Co(II)) have

been considered highly effective in activating PMS, but their toxicity and the difficulty of recovering Co(II) after reaction have hindered their widespread application [9]. The less toxic ferric ions (Fe(II)) have also been widely used to activate PMS. Nonetheless, factors such as pH operating conditions, challenging recovery, and the formation of iron sludges restrict their application [10]. Hence, the development of an efficient transition-metal-based heterogeneous catalyst to activate PMS for wastewater treatment emerges as a strategy. For example, Yang et al. reported that $CoFe_2O_4$ exhibited good PMS activation ability to decompose 2,4-dichlorophenol [11]; therefore, single-atom catalysts were synthesized and used for persulfate-based advanced oxidation processes [12].

Layered double hydroxides (LDHs) have received a lot of attention in recent decades due to their unique properties, including structure stability, large surface areas, and abundant active sites [13,14]. These materials have found wide-ranging applications across various fields [15,16]. Among them, LDHs have emerged as promising PMS activators due to their positively charged host layers, highly controllable layered structure, and metallic composition [17]. Different bimetallic LDHs have been studied for PMS activation because of their simple synthesis method and high reactivity [17]. However, the adsorption capacity of this material for organic pollutants has been reported to be limited. For instance, the adsorption efficiency of RhB was lower than 2% after 2 h in the Fe/Co-LDH system, while the adsorption efficiency of Orange II reached 4.6% after 30 min in the Mn/Fe-LDH system [18,19]. As for trimetallic LDH, Co/Fe/Ni-LDH and Cu/Co/Fe-LDH [20,21] have also been investigated for PMS activators for efficient dye pollutants degradation. However, the presence of Co in most trimetallic LDHs poses health and environmental risks due to its high toxicity and carcinogenic potential, even at low concentrations [22]. Therefore, there is a pressing need for the development of environmentally friendly trimetallic LDH catalysts. Furthermore, the Mg-based LDH found in nature is frequently used as an adsorbent due to its robust properties [23]. The presence of Mg in LDH may generate a significant number of basic sites, thereby enhancing their adsorption capacity. It has been observed that Mg-based LDHs exhibit superior stability compared to their counterparts, where substitution with Co^{2+}, Ni^{2+}, or Zn^{2+} ions has been found to decrease their thermal stability [24]. In addition, Mg-based LDHs have also been applied in catalysis and photoreduction [25]. Fe/Mn/Mg_2-LDH, with its well lamellar structure, has shown promise as a good adsorbent for phosphate and Pb(II) [26,27]. However, limited studies have investigated its potential for PMS activation. Furthermore, while much attention has been directed toward the activation ability of PMS/PS in LDH-based systems, the adsorption capacity, despite its pivotal role in pollutant removal, has often been overlooked.

In this study, Fe/Mn/Mg_2-LDH was synthesized and used both as an adsorbent for organic pollutants and as a catalyst to activate PMS, thereby generating oxygen species (ROS). The synthesized materials were well characterized by X-ray diffraction (XRD), Fourier-transform infrared spectroscopy (FTIR), Brunauer–Emmett–Teller (BET) surface area analysis, as well as scanning electron microscopy with energy-dispersive X-ray spectroscopy (SEM-EDS). The widely used azo industrial dye, Orange II, was selected as the simulated organic pollutant to investigate the pollutant degradation capability in the Fe/Mn/Mg_2-LDH/PMS system. Comparative studies on the removal of Orange II in various LDHs/PMS systems were performed. At the same time, detailed investigations were carried out to explore the impacts of reaction parameters (PMS concentration, LDH dosage, initial pH, coexisting anions, and different humic acids) on the reaction. In addition, the removal mechanism of Orange II in the Fe/Mn/Mg_2-LDH/PMS system was conducted through quenching experiments, electron paramagnetic resonance spectroscopy (EPR) experiments, and X-ray photoelectron spectroscopy (XPS) analyses. The adsorption experiment was performed with a particular focus on quantifying the oxidation and adsorption process involved in the removal of Orange II. The reusability of Fe/Mn/Mg_2-LDH was evaluated, and the removal of different pollutants in the Fe/Mn/Mg_2-LDH/PMS system was also assessed. This work presents a novel, valuable, and feasible technology for treating refractory pollutants in wastewater.

2. Results

2.1. Characterization

The XRD patterns of different samples are shown in Figure 1a. Fe/Mn/Mg_2-LDH exhibits the characteristic peaks at 11.04°, 19.06°, 22.08°, 33.69°, 38.34°, and 59.30°, which could be indexed as the reflections of the (003), (001), (006), (009), (015), and (110) planes, respectively. It could be inferred as a typical LDH structure, consistent with the published data [26]. Moreover, no obvious impurities were found in the Fe/Mn/Mg_2-LDH. The XRD patterns of fresh Fe/Mn/Mg_2-LDH slightly changed after treating it with Orange II. The intensity of the peaks at the (003) and (110) planes became weaker. The decrease in the (003) basal peak intensity could be due to the decrease in crystallite size (Table S1), calculated using the Sherrer equation (from 10.93 to 10.52 nm). The decrease in the (110) peak intensity is possibly attributed to the oxidation of Mn^{2+} by PMS, leading to a decrease in the bonding distance of the cations (since the ionic radii of Mn^{2+}, Mn^{3+}, and Mn^{4+} are 0.091, 0.071, and 0.052 nm, respectively) [28].

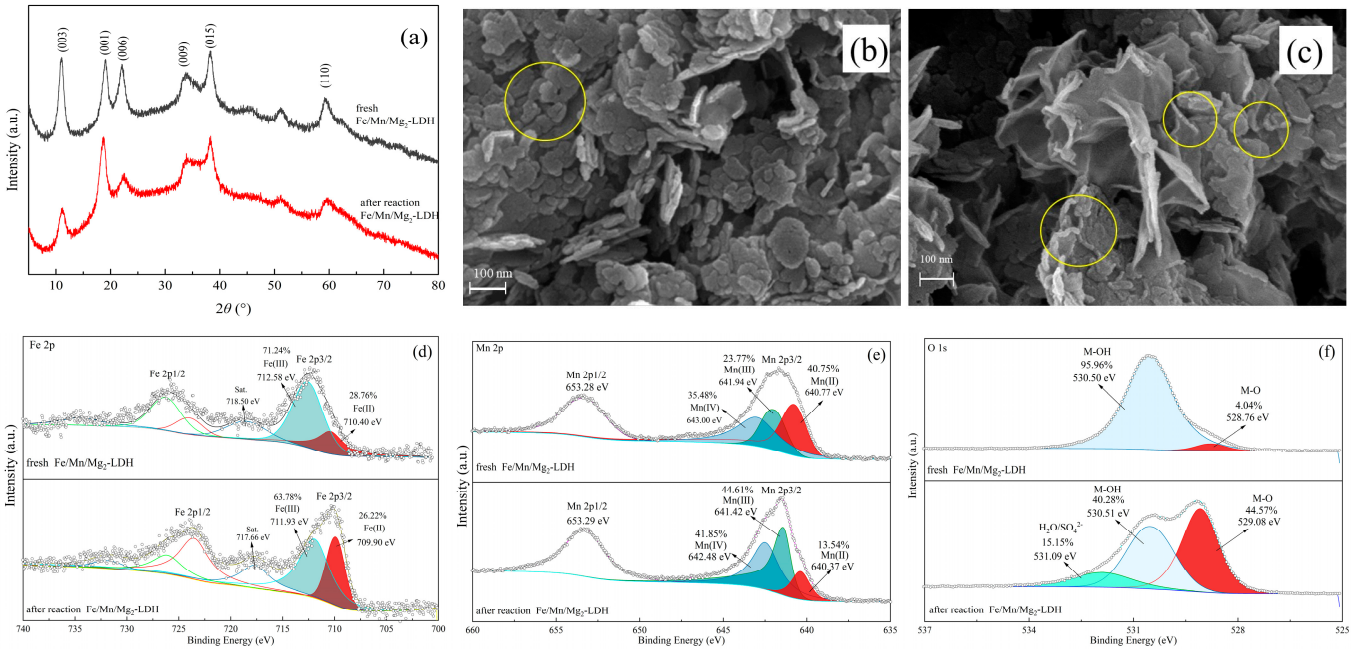

Figure 1. Characterization of catalysts (**a**) XRD patterns; (**b**) SEM image of fresh Fe/Mn/Mg_2-LDH; (**c**) SEM image of Fe/Mn/Mg_2-LDH after reaction; (**d**) Fe 2p XPS spectra (before and after reaction); (**e**) Mn 2p XPS spectra (before and after reaction); and (**f**) O 1s XPS spectra (before and after reaction).

The basal spacing (d) of the d_{110} and d_{003} planes, calculated using the Bragg equation, were 0.801 nm and 0.156nm, respectively. Hence, the crystallographic parameters a and c of the LDH phase can be calculated, assuming a hexagonal crystal system where $a = 2 \times d_{110}$ and $c = 3 \times d_{003}$ [29]. The distance between cations in the layers was 0.312 nm, which decreased to 0.308 m due to the corresponding oxidation state change during the activation process. In addition, the parameter c decreased from 2.403 nm to 2.277 nm, indicating that the attractive electrostatic forces between the layer and their interlayer became weaker [30].

The FTIR spectra of Fe/Mn/Mg_2-LDH before and after the reaction show no significant difference, indicating that the Fe/Mn/Mg_2-LDH has good stability for treating simulated Orange II wastewater (Figure S1). An analysis of the FTIR characterization is provided in the Supplementary Materials (Text S1). The presence of Fe, Mn, and Mg was confirmed in the EDS, with atomic percentage compositions of 18.0%, 23.4%, and 20.4%, respectively (Figure S2). The calculated Fe/Mn/Mg molar ratio is 1:1.3:2.4, which aligns with the designed element ratio in the synthesis experiments; however, the ratio of Mn and Mg decreased after the reaction, which could be due to the metal-leaching process. The leaching

experiment results confirm this hypothesis (Figure S3). Moreover, the SEM images of Fe/Mn/Mg_2-LDH before and after the reaction are given in Figure 1b,c. The characteristic sheet morphology of the LDHs was maintained after the reaction, and no obvious changes were observed [15]. Moreover, smaller-sized particles were observed after the reaction as indicated in the yellow circles. Particle size analysis indicated that the D_{50} value of the sample decreased from 5.467 μm to 4.595 μm (Figure S4). Additionally, the specific surface area of Fe/Mn/Mg_2-LDH increased from 69.31 ± 0.18 m^2/g to 226.41 ± 0.66 m^2/g (Figure S5), likely due to the reduction in particle size. The average pore diameter decreased from 12.67 nm to 7.73 nm. The decrease in the particle size indicated that the activation process probably caused some disruption to the structure of Fe/Mn/Mg_2-LDH. However, the reduced particle size might be conducive to the exposure of the active sites to improve the catalytic performance of the catalyst, leading to the high removal efficiency of Orange II.

XPS measurement was employed to analyze the valence changes of Mn, Fe, and O at the surface of Fe/Mn/Mg_2-LDH before and after the reaction. The full survey scan spectra of Fe/Mn/Mg_2-LDH show no obvious changes (Figure S6), indicating the stability of Fe/Mn/Mg_2-LDH. In the high-resolution spectrum of Fe 2p in the fresh Fe/Mn/Mg_2-LDH, there are two peaks located at 711.99 eV and 725.86 eV, corresponding to the binding energies of Fe 2p3/2 and Fe 2p1/2, respectively (Figure 1d) [19]. Moreover, the Fe 2p3/2 peak can be fitted to two peaks with the binding energies of 711.93 eV and 709.90 eV, corresponding to Fe(III) and Fe(II), respectively. The relative contents of Fe(III) and Fe(II) are calculated to be 71.24% and 28.76%, respectively, suggesting that Fe(III) is the dominant species in the fresh Fe/Mn/Mg_2-LDH. The Fe(III) ratio slightly decreases from 71.24% to 63.78% after reaction. Moreover, the high-resolution spectra of Mn 2p of Fe/Mn/Mg_2-LDH before and after the reaction are shown in Figure 1e. The Mn 2p3/2 in the fresh Fe/Mn/Mg_2-LDH can be fitted to three peaks at binding energies of 640.77 eV, 641.94 eV, and 643.00 eV, corresponding to Mn(II), Mn(III), and Mn(IV), respectively [19]. Furthermore, the relative contents of Mn(II), Mn(III), and Mn(IV) are calculated to be 40.75%, 23.77%, and 35.48%, respectively. Similarly, the ratio of Mn(II) decreases from 40.75% to 13.54% after reaction. This result indicates that the surface Fe/Mn elements participate in the PMS activation process, resulting in the change in their valence state [31]. Additionally, the high-resolution spectrum of O 1s peak of the fresh catalyst can be deconvoluted into two at the binding energies of 528.76 eV and 530.50 eV, corresponding to metal oxide (M-O) and metal hydroxide (M-OH), respectively (Figure 1e) [19]. A new deconvoluted O 1s peak appears at 531.09 eV, assigned to H_2O/SO_4^{2-} [19]. It is noted that the relative content of M-OH decreased dramatically after the reaction, which aligned with the observation from the FTIR spectra. This decrease suggests the involvement of metal hydroxide in the redox reaction process. In addition, the high-resolution spectrum of C 1s shows no difference before and after the reaction. No new C peaks of the contaminate were observed, which indicates that although the LDH has good adsorption capacity, the adsorbed Orange II was degraded in the reaction and the byproducts did not adsorb on its surface.

2.2. Removal of Orange II by Adsorption and Oxidation Processes

Initially, we studied the adsorption of Orange II using synthesized LDHs in the absence of PMS to differentiate between adsorption and oxidation processes in its removal. Subsequently, we investigated the synergy of adsorption and oxidation processes in the presence of PMS. To calculate and compare the removal efficiency of Orange II in the different systems, we employed a pseudo-first-order equation to process the kinetic data. This equation, denoted as Equation (1), can be expressed as follows:

$$-\ln(C_t/C_0) = k_{obs}\, t \quad (1)$$

where C_0 and C_t represent the initial concentration of Orange II and the concentration at reaction time t, respectively. k_{obs} represents an apparent first-order reaction rate constant. The value of k_{obs} (min^{-1}) is calculated from the slope of the plots of $\ln(C_t/C_0)$ versus t. This equation is specifically applied to data collected within the initial 15 min.

Since both adsorption and oxidation processes exist in the presence of PMS, hence the apparent rate constant of the oxidation part ($k_{obs(ox)}$) can be calculated using the following expression:

$$k_{obs(ox)} = k_{obs(Overall)} - k_{obs(ads)} \quad (2)$$

where $k_{obs(Overall)}$ and $k_{obs(ads)}$ identify the overall apparent rate constant in the presence of PMS and the apparent rate constant of the adsorption part in the absence of PMS, respectively.

Figure 2a shows the Orange II adsorption kinetics by various LDHs under their optimal conditions. The study of the effects of pH and material dosage on the adsorption of Orange II can be obtained in Figure S8. No adsorption of Orange II is observed after 60 min by all bimetallic LDHs (with molar ratios of Fe/Mn ranging from 1:1 to 1:8), suggesting a limited contribution of Orange II adsorption by the bimetallic LDH. This is consistent with the published studies [19]. In contrast, two trimetallic LDHs (FeMnMg-LDH and Fe/Mn/Mg_2-LDH) exhibited higher adsorption capacities, with the Orange II removal rate of 48.4% and 56.3% within 60 min, respectively. Fe/Mn/Mg_2-LDH can efficiently adsorb anions or organic compounds via ion exchange, electrostatic attraction, and surface complexation processes, which contribute to its hydrotalcite-like structure [32]. Figure 2b shows the Orange II removal kinetics in the presence of PMS. For the bimetallic LDHs, the Orange II removal rate decreased from 97.6% to 14.0% as the Fe/Mn molar ratio varied from 1:1 to 1:8. The best molar ratio for Fe/Mn is determined to be 1:1. For the trimetallic LDHs, the removal efficiency in the Fe/Mn/Mg_2-LDH/PMS system is much higher compared to the Fe/Mn/Mg-LDH/PMS system. The Orange II removal rate reached 98.7% within 30 min in Fe/Mn/Mg_2-LDH/PMS. The overall values of k_{obs} for the different LDHs/PMS systems are calculated and presented in Figure 2c and Table S2. Fe/Mn/Mg_2-LDH/PMS system demonstrates a high removal efficiency (97.6%). The $k_{obs(Overall)}$, $k_{obs(ads)}$, and $k_{obs(ox)}$ were calculated to be 0.165, 0.035, and 0.130 min^{-1}, respectively, in this system, which is higher than the others. The optimal Fe and Mn molar ratio of 1:1 is critical, as activation can be negatively impacted if the ratio deviates from this value [19]. Furthermore, the introduction of Mg enhances the adsorption and PMS activation capacity [33]. Therefore, Fe/Mn/Mg_2-LDH emerges as a promising candidate for Orange II removal from water. This result shows the synergistic mechanism of adsorption and oxidation in Fe/Mn/Mg_2-LDH/PMS.

2.3. Effects of Different Parameters on the Removal of Orange II

To optimize the conditions of the removal of Orange II by the Fe/Mn/Mg_2-LDH/PMS system, various parameters such as initial solution pH, Fe/Mn/Mg_2-LDH dosage, PMS concentration, co-existing anions, and humic acid were investigated.

The effect of pH on the removal of Orange is shown in Figure 3a. The Fe/Mn/Mg_2-LDH/PMS system exhibits a wide pH adaptability, and the Orange II can be efficiently removed at a wide pH range from 4.0 to 9.0. Compared with the adsorption processes (Figure S9a,b), the $k_{obs(Overall)}$ of Orange II removal increases from 0.088 min^{-1} to 0.188 min^{-1} with the pH increasing from 4.0 to 9.0 (Figure S10a). This might be because the catalyst decomposes at a lower pH, leading to the high rate of leaching of Mn and Fe from the catalysts and a decrease in the number of active sites for PMS activation (Figure S3). This can also be because the higher pH is favorable to the activation of PMS [32].

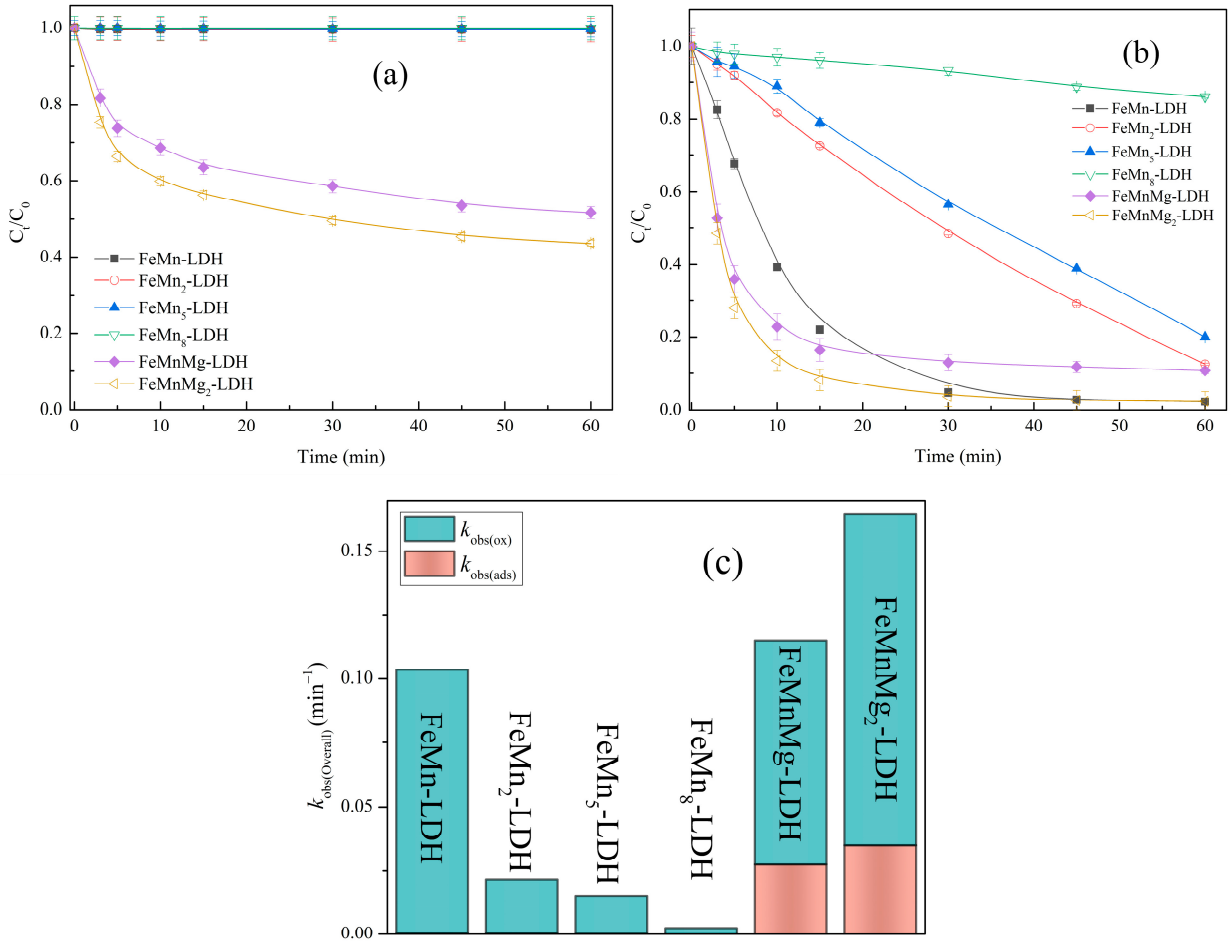

Figure 2. The removal of Orange II in different LDH suspensions in the absence and presence of PMS. (**a**) Adsorption of Orange II by different LDH. (**b**) The removal efficiency of Orange II in different LDH/PMS systems. (**c**) The k_{obs} in different LDH/PMS systems (Experimental conditions: bimetallic materials system: [bimetallic materials] = 0.20 g L^{-1}, [PMS] = 0.5 mmol L^{-1}, [Orange II]$_0$ = 50 μmol L^{-1}, pH 6.0; trimetallic materials system: [trimetallic materials] = 0.16 g L^{-1}, [PMS] = 0.5 mmol L^{-1}, [Orange II]$_0$ = 50 μmol L^{-1}, pH 7.0).

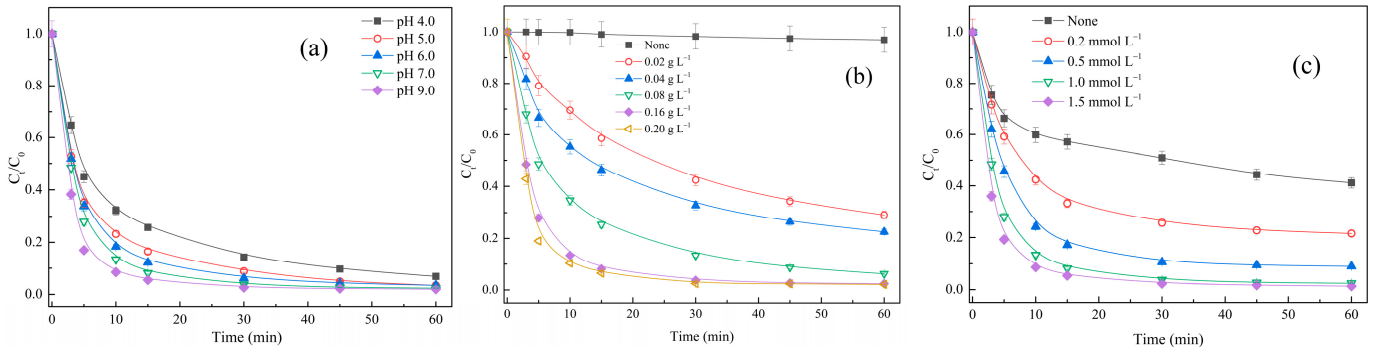

Figure 3. Effects of (**a**) pH; (**b**) Fe/Mn/Mg$_2$-LDH dosage; and (**c**) PMS concentration on the removal of Orange II in Fe/Mn/Mg$_2$-LDH/PMS system. (Experimental conditions: (**a**) [Fe/Mn/Mg$_2$-LDH] = 0.16 g L^{-1}, [Orange II]$_0$ = 50 μmol L^{-1}, [PMS] = 1.0 mmol L^{-1}; (**b**) [Orange II]$_0$ = 50 μmol L^{-1}, [PMS] = 1.0 mmol L^{-1}, pH 7.0; (**c**) [Fe/Mn/Mg$_2$-LDH] = 0.16 g L^{-1}, [Orange II]$_0$ = 50 μmol L^{-1}, pH 7.0).

The effects of the dosage of Fe/Mn/Mg_2-LDH are shown in Figure 3b. The removal efficiency of Orange II increases with the addition of Fe/Mn/Mg_2-LDH. As shown in Figure S10b, the value of k_{obs} increases from 0.035 min^{-1} to 0.165 min^{-1} with the increasing amount of the catalyst from 0.02 to 0.16 g L^{-1} before reaching a plateau. This is attributed to the higher amount of active sites for the PMS activation as well as the adsorption sites, resulting in improved removal of Orange II [33].

The effect of PMS concentration is shown in Figure 3c. The removal efficiency increases from 78.5% to 98.0% after 60 min with increasing PMS concentration from 0.2 to 1.0 mmol L^{-1}, whereas increasing the PMS concentration to 1.5 mmol L^{-1} only slightly enhances the removal efficiency. The same results can be found in the value of k_{obs} (Figure S10c), which are attributed to the limited Fe/Mn/Mg_2-LDH dosage. It is well known that PMS is the source of radicals, and increasing the concentration of PMS is effective in promoting the removal of Orange II within a certain range of concentrations. But excessive PMS could directly react with $SO_4^{\bullet-}$, $HO^{\bullet}$ to produce $SO_5^{\bullet-}$ (Equations (3) and (4)), which has a lower redox potential of 1.1 V, resulting in the unsatisfactory removal of Orange II [34–36].

$$HSO_5^- + SO_4^{\bullet-} \rightarrow SO_4^{2-} + SO_5^{\bullet-} + H^+ \quad (3)$$

$$HSO_5^- + HO^{\bullet} \rightarrow H_2O + SO_5^{\bullet-} \quad (4)$$

The coexisting anions chloride (Cl^-), carbonate (CO_3^{2-}), and phosphate (PO_4^{3-}) were studied, as shown in Figure 4. In the presence of chloride ions (Cl^-), the removal efficiency of Orange II is not affected (as shown in Figure 4a). The value of k_{obs} increases from 0.630 min^{-1} to 0.782 min^{-1}, along with the increase in Cl^- concentration (Figure S11). Cl^- can directly react with HSO_5^- to generate Cl_2 and HOCl (Equations (5) and (6)) [37], which has been proven to be an effective oxidant for dye decolorization [38]. Meanwhile, the Orange II removal is inhibited in the presence of CO_3^{2-}, and PO_4^{3-}, due to the generation of lower reactive radicals ($HCO_3^{\bullet}/CO_3^{\bullet-}$ [39] and $HPO_4^{\bullet-}/H_2PO_4^{\bullet}$ [40]), as shown in Equations (7)–(11). In addition, CO_3^{2-} and PO_4^{3-} exhibit competition with Orange II towards the adsorptive site as well [41].

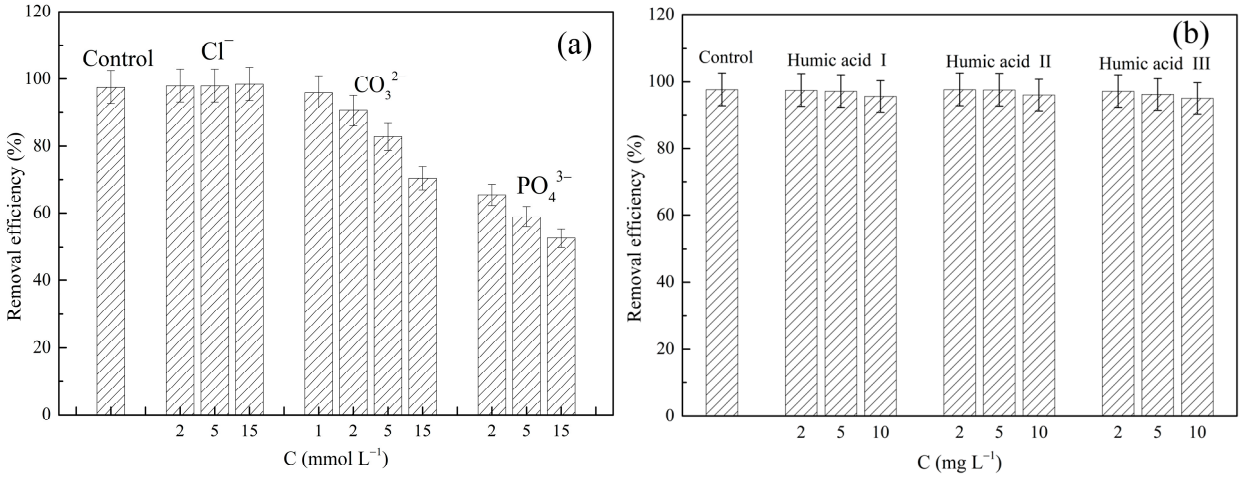

Figure 4. Effect of (**a**) co-existing anions (Cl^-, CO_3^{2-}, and PO_4^{3-}) and (**b**) different humic acids (Humic acid I: IHSS Elliott soil Humic Acid standard IV; Humic acid II: IHSS Leonardite Humic Acid standard; Humic acid III: IHSS Pahokee Peat Humic Acid standard) on the removal of Orange II in Fe/Mn/Mg_2-LDH/PMS system. (Experimental conditions: [Fe/Mn/Mg_2-LDH] = 0.16 g L^{-1}, $[Orange\ II]_0$ = 50 μmol L^{-1}, [PMS] = 1.0 mmol L^{-1}, pH 7.0).

Since humic acid (HA) is commonly found in natural water environments, in this study, three different HA at different concentrations were used to study the effect on orange II removal efficiency, as shown in Figure 4b. A slight decrease in Orange II removal

efficiency is observed when the HA concentration increases. As shown in Figure S12, the k_{obs} value decreases from 0.630 min^{-1} to 0.450 min^{-1} with increasing concentrations of HA II, which indicates the inhibition of HA upon Orange II removal. This is likely because HA is adsorbed onto the surface of the Fe/Mn/Mg_2-LDH, occupying the adsorptive sites and reducing the adsorption of Orange II on Fe/Mn/Mg_2-LDH [42]. Moreover, it might be due to the competition between humic acid and Orange II for trapping the reactive species in the system. Conversely, phenols and quinones present in humic acid might stimulate the decomposition of PMS and generate free radicals [43]. Therefore, the removal of Orange II is slightly inhibited in the presence of HA in the Fe/Mn/Mg_2-LDH/PMS system.

$$HSO_5^- + Cl^- \rightarrow SO_4^{2-} + HOCl \quad (5)$$

$$HSO_5^- + 2Cl^- + H^+ \rightarrow SO_4^{2-} + H_2O + Cl_2 \quad (6)$$

$$CO_3^{2-} + SO_4^{\bullet-} \rightarrow SO_4^{2-} + CO_3^{\bullet-} \quad (7)$$

$$HCO_3^- + SO_4^{\bullet-} \rightarrow SO_4^{2-} + HCO_3^{\bullet} \quad (8)$$

$$CO_3^{2-} + HO^{\bullet} \rightarrow CO_3^{\bullet-} + OH^- \quad (9)$$

$$HPO_4^{2-} + SO_4^{\bullet-} \rightarrow SO_4^{2-} + HPO_4^{\bullet-} \quad (10)$$

$$H_2PO_4^- + HO^{\bullet} \rightarrow HPO_4^{\bullet} + OH^- \quad (11)$$

2.4. Reactive Species Analysis

To study the reactive species involved in the oxidation of Orange II in the Fe/Mn/Mg_2-LDH/PMS system, electron paramagnetic resonance spectroscopy (EPR) was employed to identify the presence of free radicals. As shown in Figure 5a, the EPR signals of DMPO-OH, DMPO-SO_4^- and DMPO-O_2^-, and TEMP-O_2 adducts are observed, which indicate that $HO^{\bullet}$, $SO_4^{\bullet-}$, $O_2^{\bullet-}$ and $^1O_2$ were all generated in Fe/Mn/Mg_2-LDH/PMS system.

To determine the contributions of different reactive species to the removal of Orange II, different radical scavengers were used as probes of the different radicals. Methanol (MeOH), tert-butyl alcohol (TBA), phenol, superoxide dismutase (SOD), Furfuryl alcohol (FFA), and dimethyl sulfoxide (DMSO) were used as probes for $SO_4^{\bullet-}$ in solution ($SO_4^{\bullet-}{}_{aq}$), $HO^{\bullet}$ in solution ($HO^{\bullet}{}_{aq}$), $SO_4^{\bullet-}$ and $HO^{\bullet}$ at the surface ($SO_4^{\bullet-}{}_{ads}$ and $HO^{\bullet}{}_{ads}$), $O_2^{\bullet-}$, $^1O_2$, and high-valent metal, respectively [44,45]. The reaction rate constants of those scavengers with different radicals are provided in Table S2. It is noteworthy that TBA and MeOH, both are hydrophilic and can only quench radicals in the solution, specifically $SO_4^{\bullet-}{}_{aq}$ and $HO^{\bullet}{}_{aq}$ [36]. On the other hand, phenol is hydrophobic and capable of scavenging the radicals on the surface, i.e., $SO_4^{\bullet-}{}_{ads}$ and $HO^{\bullet}{}_{ads}$ [46]. The inhibition ratio of different scavengers on Orange II oxidation was calculated by the following expression [46]:

$$\text{Inhibition ratio } (\%) = [(k_{obs(overall)} - k_{obs(ads)} - k_{obs(overall)}')/(k_{obs(overall)} - k_{obs(ads)})] \times 100\% \quad (12)$$

where $k_{obs(overall)}$ and $k_{obs(overall)}'$ are the apparent rate constant of Orange II removal in the absence and the presence of scavengers, respectively.

As shown in Figure 5b, In the presence of MeOH, TBA, and SOD, no inhibition of Orange II removal is observed, indicating that $SO_4^{\bullet-}{}_{aq}$, $HO^{\bullet}{}_{aq}$, and $O_2^{\bullet-}$ are not the main reactive species involved in the oxidation process. Alternatively, FFA, phenol, and DMSO can inhibit the adsorption as well as the oxidation of Orange II at pH 7.0 in the Fe/Mn/Mg_2-LDH/PMS system. Moreover, the removal of Orange II is highly inhibited (94%) in the presence of phenol, suggesting that the $SO_4^{\bullet-}{}_{ads}$ and $HO^{\bullet}{}_{ads}$ play important roles in the system. In the presence of FFA and DMSO, the oxidation was inhibited at around 94% and 96%, which indicates that the contribution of $^1O_2$ and high-valent metals is negligible in this system. Hence, these results illustrate that $SO_4^{\bullet-}{}_{ads}$ and $HO^{\bullet}{}_{ads}$ are the main reactive species that can lead to efficient Orange II oxidation in the system.

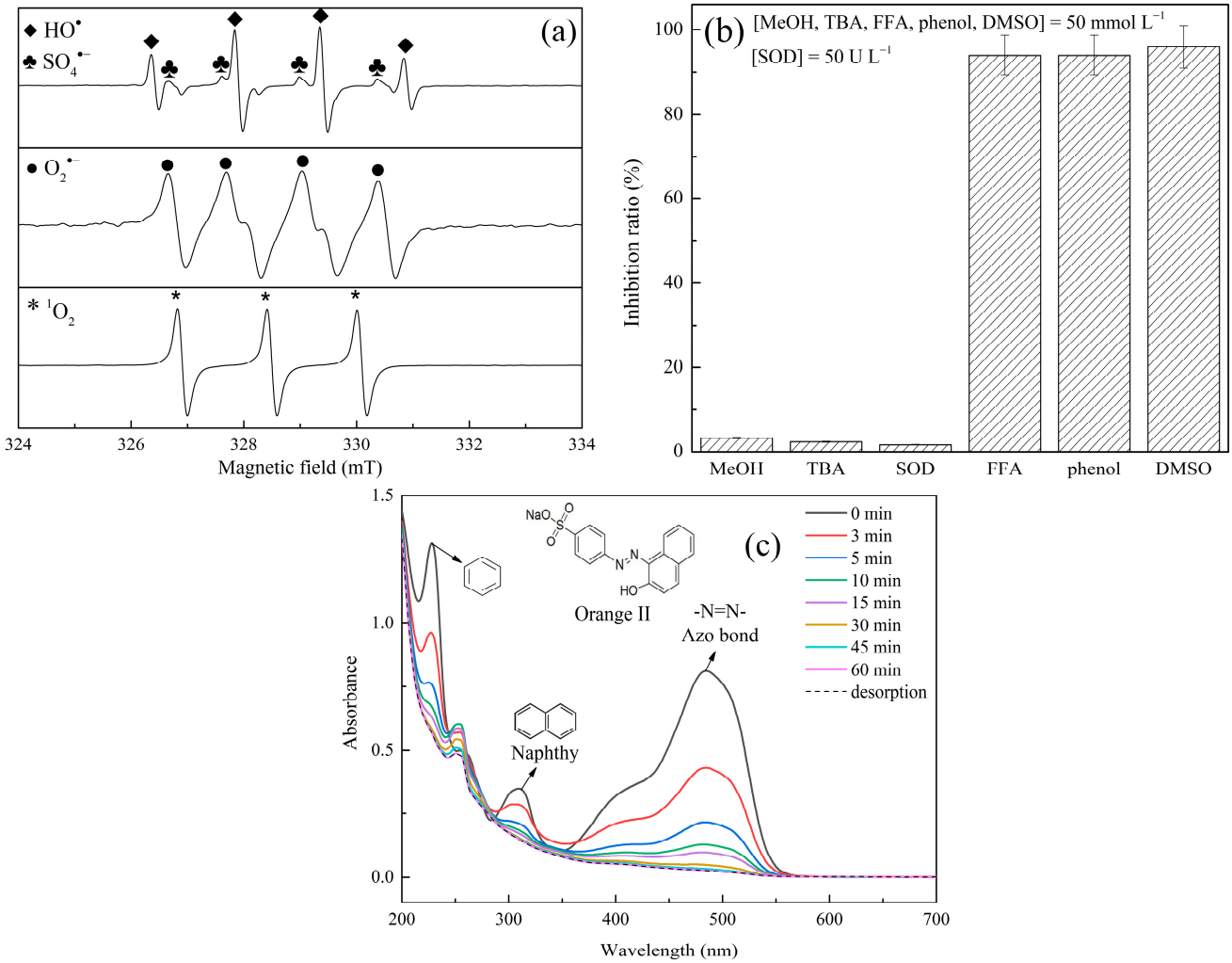

Figure 5. (**a**) EPR spectra of DMPO-OH, DMPO-SO_4^-, DMPO-O_2^- and TEMP-O_2; (**b**) Inhibition ratio of scavengers on the removal of Orange II; (**c**) Absorbance spectra of Orange II removal at different times in Fe/Mn/Mg_2-LDH/PMS system (Experimental conditions: (**a**) [Fe/Mn/Mg_2-LDH] = 0.16 g L^{-1}, [PMS] = 1.0 mmol L^{-1}, [DMPO/TEMP] = 50 mmol L^{-1}, pH 7.0; (**b**) [Fe/Mn/Mg_2-LDH] = 0.16 g L^{-1}, [Orange II]$_0$ = 50 μmol L^{-1}, [PMS] = 1.0 mmol L^{-1} pH 7.0; (**c**) [Fe/Mn/Mg_2-LDH] = 0.16 g L^{-1}, [Orange II]$_0$ = 50 μmol L^{-1}, [PMS] = 1.0 mmol L^{-1}, pH 7.0).

2.5. Mechanistic Insights into Orange II Oxidation

To explore the evolution of molecular structure characteristics of Orange II in the Fe/Mn/Mg_2-LDH/PMS system, the UV–Vis spectra of the different reaction times were recorded by UV–Vis spectrometry, as shown in Figure 5c. The characteristic peaks observed at 484 and 422 nm are attributed to the azo linkage of Orange II, corresponding to its hydrazine and azo forms, respectively [47]. Furthermore, the peaks located at 228 and 309 nm are assigned to the naphthalene and benzene rings of Orange II, respectively [48]. The weakening of the absorption peaks at 484, 422, 309, and 228 nm is observed, suggesting that the azo bond, naphthalene, and benzene rings are gradually attacked during the reaction. On the contrary, an elevation in the peak at 251 nm is noted, indicating the generation of intermediate products within the system [49]. To study if Orange II adsorbed on Fe/Mn/Mg_2-LDH surface is degraded by generated reactive species in the system, hydrochloric acid (HCl) was employed to desorb Orange II from the surface [50], and a UV–Vis spectrum was used to analyze the desorption solution. As shown in Figure 5c, the dashed line shows no more difference with the magenta solid line (after 60 min of reaction). This indicates that adsorbed Orange II is most likely oxidized by the generated surface

$SO_4^{\bullet-}{}_{ads}$ and $HO^{\bullet}{}_{ads}$ radicals. The total organic carbon (TOC) results showed that the TOC concentration in the system decreased by 57.2% after two hours of reaction. This indicates that the generated surface $SO_4^{\bullet-}{}_{ads}$ and $HO^{\bullet}{}_{ads}$ radicals in the system can mineralize the Orange II, which is finally converted to CO_2 and H_2O.

According to the overall results and the published literature, the potential mechanism of the removal of Orange II in the Fe/Mn/Mg_2-LDH/PMS system is proposed and shown in Figure 6. The adsorption and oxidation processes are involved in the Orange II removal. Orange II is adsorbed and then oxidized by the $SO_4^{\bullet-}{}_{ads}$ and $HO^{\bullet}{}_{ads}$ radicals generated on the catalyst surface. Those radicals directly attack the azo bond, naphthalene, and benzene rings of Orange II. In terms of the generation of reactive species in the system, both Mn(II)/Fe(II) on the surface of Fe/Mn/Mg_2-LDH activate HSO_5^- to generate $SO_4^{\bullet-}{}_{ads}$ and/or $HO^{\bullet}{}_{ads}$ and produce Mn(III)/Fe(III) via electrons donation (Equations (13)–(16)) [51,52]. Then, the generated Mn(III)/Fe(III) can react with HSO_5^- to produce $O_2^{\bullet-}$ and regenerate Mn(II)/Fe(II) (Equations (17) and (18)) [53]. Given the higher standard redox potential of Mn(III)/Mn(II) (1.51 V) compared to that of Fe(III)/Fe(II) (0.77 V) [19], Fe(II) can directly reduce Mn(III) to Mn(II) (Equation (19)) [6]. The generated $O_2^{\bullet-}$ can react with H_2O to produce $^1O_2$ (Equation (20)) [54]. Furthermore, $SO_4^{\bullet-}$ can transform into $HO^{\bullet}$ via Equations (21) and (22) [55,56]. The regeneration of the active sites of Fe/Mn/Mg_2-LDH enables the activation cycle to continue until the HSO_5^- is completely consumed [56,57].

$$Fe(II) + HSO_5^- \rightarrow Fe(III) + HO^{\bullet} + SO_4^{2-} \quad (13)$$

$$Fe(II) + HSO_5^- \rightarrow Fe(III) + SO_4^{\bullet-} + OH^- \quad (14)$$

$$Mn(II) + HSO_5^- \rightarrow Mn(III) + SO_4^{2-} + HO^{\bullet} \quad (15)$$

$$Mn(II) + HSO_5^- \rightarrow Mn(III) + SO_4^{\bullet-} + OH^- \quad (16)$$

$$Fe(III) + HSO_5^- + H_2O \rightarrow Fe(II) + SO_4^{2-} + O_2^{\bullet-} + 3H^+ \quad (17)$$

$$Mn(III) + HSO_5^- + H_2O \rightarrow Mn(II) + SO_4^{2-} + O_2^{\bullet-} + 3H^+ \quad (18)$$

$$Fe(II) + Mn(III) \rightarrow Fe(III) + Mn(II) \quad (19)$$

$$2O_2^{\bullet-} + 2H_2O \rightarrow {}^1O_2 + H_2O_2 + 2OH^- \quad (20)$$

$$SO_4^{\bullet-} + OH^- \rightarrow SO_4^{2-} + HO^{\bullet} \quad (21)$$

$$SO_4^{\bullet-} + H_2O \rightarrow SO_4^{2-} + HO^{\bullet} + H^+ \quad (22)$$

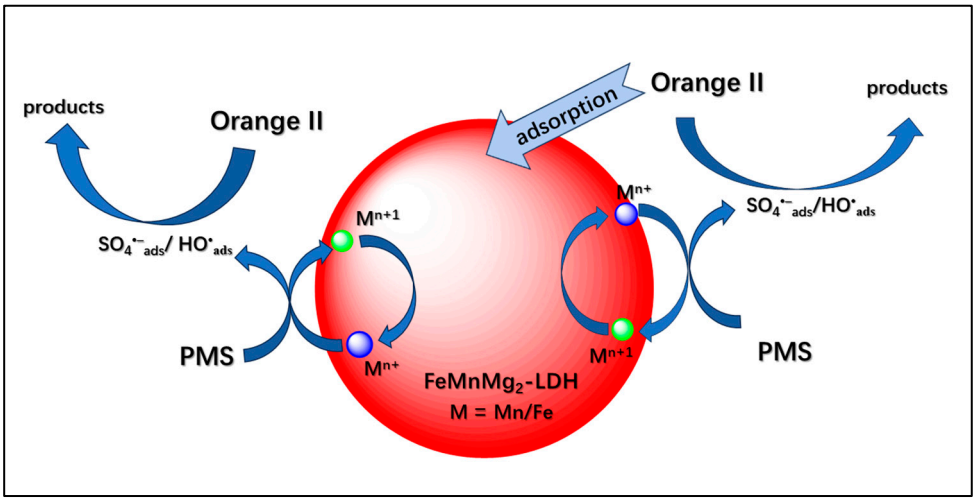

Figure 6. The proposed mechanism of Orange II removal in Fe/Mn/Mg_2-LDH/PMS system.

2.6. Applications

To evaluate the reusability of the catalyst, the fresh PMS and Orange II solutions were added into a suspension under identical conditions (0.16 g L^{-1} Fe/Mn/Mg_2-LDH, pH of 7.0). Even after five consecutive runs, the removal efficiency of Orange II remained at 90% in 60 min. A slight decrease in Orange II removal efficiency can be observed compared with the initial run. The results illustrated the high stability of the Fe/Mn/Mg_2-LDH/PMS system. The slight decrease is due to the formation of the by-products in the system, which has competition with Orange II for the consumption of ROS in the system. To assess the broad applicability of the Fe/Mn/Mg_2-LDH/PMS system, various organic contaminants, including acetaminophen (APAP), 4-chloroaniline (p-CAN), N,N-dimethylaniline (DMA), benzoic acid (BA), and benzene were treated using this system. Figure 7b shows that all selected contaminants have been degraded by the Fe/Mn/Mg_2-LDH/PMS system in 60 min with different removal efficiencies (Orange II: 98.0%; benzene: 99.8%; APAP: 100.0%; DMA: 100.0%; p-CAN: 100.0%; BA: 41.0%). A good removal efficiency can be obtained for all the contaminants except for BA. This might be because contaminants containing electron-withdrawing groups (such as –COOH) are less efficient to be oxidized by $SO_4^{\bullet-}$ [58]. Overall, the system exhibits promising removal capabilities for a variety of contaminants and has specific potential applications in the treatment of contaminants.

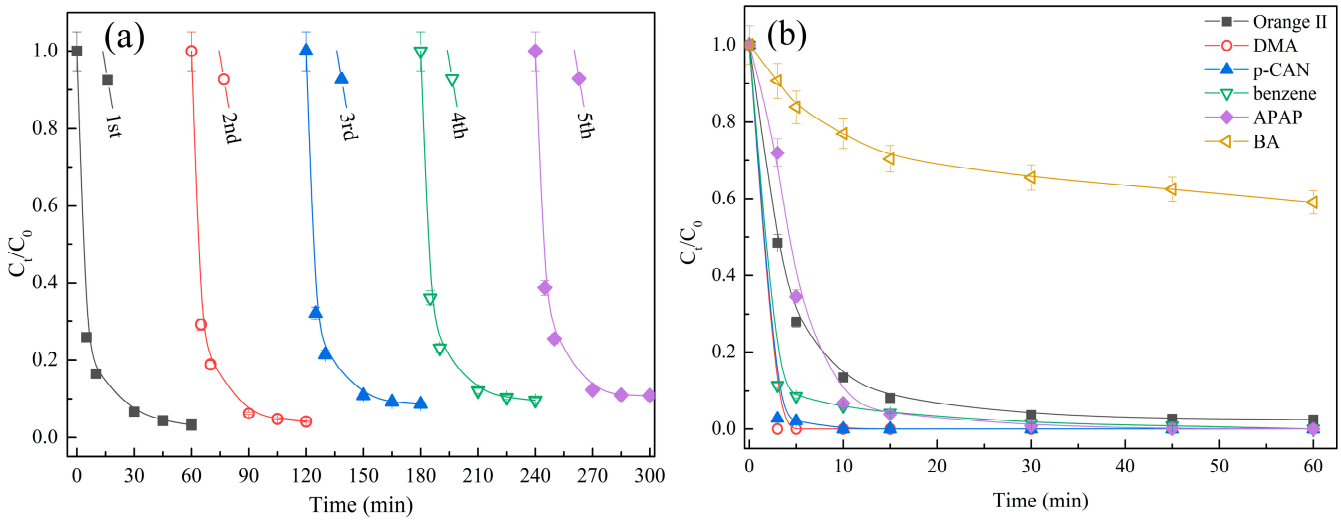

Figure 7. (**a**) The removal efficiency of Orange II over time in sequential experiments upon multiple additions of 2.5 mL 5.0 mmol L^{-1} Orange II and 5.0 mL 50 mmol L^{-1} PMS solution every 60 min; (**b**) The removal of various organic contaminants in Fe/Mn/Mg_2-LDH/PMS system (Experimental conditions: [Fe/Mn/Mg_2-LDH] = 0.16 g L^{-1}, [PMS] = 1.0 mmol L^{-1}, $[Contaminants]_0$ = 50 μmol L^{-1}, pH 7.0).

3. Conclusions

In this study, an environmentally friendly catalyst, Fe/Mn/Mg_2-LDH, was successfully synthesized using the co-precipitation method. The catalyst exhibited high efficiency in the removal of Orange II in the presence of PMS. Up to 98.0% of Orange II could be removed within 60 min when PMS concentration was 1.0 mmol L^{-1}, Fe/Mn/Mg_2-LDH dosage was 0.16 g L^{-1}, and the initial Orange II concentration was 50 μmol L^{-1} at pH 7.0. Further investigations reveal that the removal of Orange II in the Fe/Mn/Mg_2-LDH/PMS system was unaffected by the changes in pH, while a higher Fe/Mn/Mg_2-LDH dosage and PMS concentration can promote the removal of Orange II. However, the presence of CO_3^2 and PO_4^{3-} inhibited the removal of Orange II. In contrast, an obvious side effect is observed in the presence of Cl^- and humic acids on the removal of Orange II in Fe/Mn/Mg_2-LDH/PMS. The removal of Orange II is involved in a synergy of adsorption and oxidation processes. The Orange II adsorbed on the catalyst surface is simultaneously

oxidized by the generated surface $SO_4^{\bullet -}{}_{ads}$ and $HO^{\bullet}{}_{ads}$ radicals in the Fe/Mn/Mg_2-LDH/PMS system. In addition, the Fe/Mn/Mg_2-LDH exhibited satisfactory reusability and stability over five cycles of recycling. This work may provide valuable insights into the potential environmental applications of trimetallic LDH. In the future, it is necessary to study its performance in treating actual wastewater containing Orange II and try to apply this catalyst in practical applications.

4. Materials and Methods

4.1. Chemicals

Potassium peroxymonosulfate ($KHSO_5 \cdot 0.5KHSO_4 \cdot 0.5K_2SO_4$) was purchased from Sigma Aldrich (Saint Louis, MO, USA). Orange II ($C_{16}H_{11}N_2NaO_4S$, >85.0%), manganese chloride, tetrahydrate (II) ($MnCl_2 \cdot 4H_2O$, 99.0%), iron trichloride, hexahydrate (III) ($FeCl_3 \cdot 6H_2O$, 99.0%), magnesium chloride, hexahydrate ($MgCl_2 \cdot 6H_2O$, 99.0%) were purchased from Shanghai Macklin Biochemical Technology Co., Ltd., Shanghai, China. Sodium hydroxide (NaOH, $\geq$96.0%) was purchased from Sinopharm Chemical Reagent Co., Ltd., Shanghai, China. All other reagents in this work are of analytic grade or higher and used without further purification. Unless otherwise stated, all the experiments were performed using milli-Q water (resistivity of 18 MΩ cm, DOC < 0.1 mg L^{-1}).

4.2. Fe/Mn/Mg_2-LDH Preparation

The following steps were taken to synthesize the Fe/Mn/Mg_2-LDH using the co-precipitation method [59]. Initially, $FeCl_3 \cdot 6H_2O$, $MnCl_2 \cdot 4H_2O$, and $MgCl_2 \cdot 6H_2O$ were dissolved in oxygen-free water with a molar ratio of $Fe^{3+}/Mn^{2+}/Mg^{2+}$ of 1:1:2 and a total metal concentration of approximately 2.0 mol L^{-1}. Subsequently, the mixed metal solution was added into a homemade reactor at a flow rate of 0.5 mL min^{-1}, while 3.0 mol L^{-1} NaOH was added at a variable flow rate to maintain the reaction pH at 10.0 ± 0.1. The mixed solution was stirred at 25.0 °C under an N_2 atmosphere for 1 h. After the preparation process, the mixed solution was allowed to age for 24 h at ambient temperature. Then, the solution was centrifuged and filtered, yielding the catalyst. The obtained catalyst was then washed with Milli-Q water three times and freeze-dried for 96 h. The preparation details of LDHs with different metal ratios were provided in Supporting Materials (Text S2).

4.3. Catalyst Characterization

The properties of Fe/Mn/Mg_2-LDH were characterized using several analytical techniques. The X-ray diffraction (XRD) patterns were recorded by a D-8 Advance diffractometer (Bruker, Karlsruhe, Germany) equipped with Cu Kα radiation (λ = 1.54056 Å). The operating voltage was set to 40 kV and the current to 30 mA. The chemical functional group information on the surface of the catalyst was analyzed by Fourier transfer infrared spectrometer (FTIR, Thermo Fisher Scientific 4700, Waltham, MA, USA) in the wavenumber range from 400 to 4000 cm^{-1} with a resolution of 4 cm^{-1}. X-ray photoelectron spectroscopy (XPS) analysis was conducted on a photoelectron spectrometer (Scientific K-Alpha, Thermo Fisher, Waltham, MA, USA) equipped with monochromatic Al Kα radiation (hυ = 1486.6 eV). The binding energy scale was calibrated using the C 1s peak at 284.8 eV as a reference. The morphology of the samples was observed using a scanning electron microscope (SEM, Zeiss Sigma 300, Oberkochen, Germany) combined with energy dispersive spectrometry (EDS, XFlash6I30, Karlsruhe, Germany). The SEM was operated at an accelerating voltage (EHT) of 10.00 kV with a resolution of 1.0 nm. Brunauer–Emmett–Teller (BET) specific surface area and mean pore diameter of the samples were used to measure the adsorption/desorption of N_2 at 77 K (BET, ASAP 2460, Norcross, GA, USA). Particle size analysis was performed on a laser diffraction particle size analyzer (Mastersizer 3000+, Malvern Panalytical, Malvern, UK), with a size range from 0.020 to 2000.000 μm.

4.4. Experimental Methods

Batch experiments were conducted in brown glass bottles (250 mL) equipped with magnetic stirring (400 rpm) at a constant water bath temperature of 25.0 °C. Orange II and PMS were added to the solution, and the solution's pH was adjusted with $HClO_4$ or NaOH solutions. The reaction was started by the addition of Fe/Mn/Mg_2-LDH. To optimize the experimental conditions, the pH (4.0, 5.0, 6.0, 7.0, and 9.0), Fe/Mn/Mg_2-LDH dosage (0.02 − 0.2 g L^{-1}), PMS (0.2 − 1.5 mmol L^{-1}), different co-existing anions (Cl^-, CO_3^{2-}, and PO_4^{3-}) at different concentrations (2, 5, and 15.0 mg L^{-1}), and humic acid (HA) at different concentration (2.0, 5.0, and 10.0 mg L^{-1}) were investigated. To determine the contributions of different reactive species in the system, quenching experiments were conducted. Methanol (MeOH), superoxide dismutase (SOD), tert-butyl alcohol (TBA), dimethyl sulfoxide (DMSO), phenol, and furfuryl alcohol (FFA) were added to the suspension at a concentration of 50 mmol L^{-1}. For the desorption experiments, 1 mL 2.5mol L^{-1} HCl was added into the system to keep the pH value around 2.0, then the mixture was stirred for 6 h to desorb the Orange II from the Fe/Mn/Mg_2-LDH surface. To assess the recyclability of Fe/Mn/Mg_2-LDH in activating PMS, the material was reused across five cycles in consecutive experiments without any regeneration treatments. Initially, a suspension containing 0.16 g L^{-1} Fe/Mn/Mg_2-LDH, 1.0 mmol L^{-1} PMS, and 50 µmol L^{-1} Orange II was prepared. For the subsequent runs, PMS and Orange II at identical dosages were intermittently added to the reaction suspension at pH 7.0 every 60 min. The samples were collected at specific time intervals and filtered through a 0.22 µm filter, and the residual Orange II in the mixture was analyzed using a UV–Vis spectrophotometer.

4.5. Analytical Methods

The concentration of Orange II was determined at a wavelength of 484 nm using UV–Vis spectrometry. The variation in PMS concentration was measured using iodine dosimetry [60]. The leaching of ferrous ions and total iron in the system was determined using the Ferrozine method [61]. The leaching of manganese ions in the Fe/Mn/Mg_2-LDH/PMS system was measured using atomic absorption spectrophotometry (AAS, TAS-990AFG, Beijing, China). The generation of radicals and $^1O_2$ was detected using an electron paramagnetic resonance spectrometer (EPR, JES-FA300, Akishima-shi, Japan). The 5,5-dimethyl-1-pyrroline-N-oxide (DMPO) was used as a spin-trapping agent for $SO_4^{\bullet-}$, $HO^{\bullet}$ and $O_2^{\bullet-}$, while 2,2,6,6-tetramethyl-4-piperidine (TEMP) was used as an $^1O_2$ trapping agent in the Fe/Mn/Mg_2-LDH/PMS system [62]. Total organic carbon (TOC) was determined using a TOC analyzer (Elementar, vario TOC select, Frankfurt, Germany).

Supplementary Materials: The following supporting information can be downloaded at: https://www.mdpi.com/article/10.3390/catal14060380/s1, Text S1: Analysis of FTIR spectra of fresh and used Fe/Mn/Mg_2-LDH; Text A2: Preparation of other LDHs used in this study; Table S1: Lattice parameters of samples of Fe/Mn/Mg_2-LDH before and after reaction; Table S2: $k_{obs(overall)}$, $k_{obs(ads)}$, and $k_{obs(ox)}$ of Orange II removal in LDHs/PMS systems at its optimal conditions; Table S3: Rate constants of ROSs and quenchers; Figure S1: FTIR spectra of Fe/Mn/Mg_2-LDH before and after reaction; Figure S2: EDS spectra of the Fe/Mn/Mg_2-LDH before and after reaction; Figure S3: Leaching of Fe (a) and Mn (b) from Fe/Mn/Mg_2-LDH during reactions at different initial pH conditions; Figure S4: The particle size distribution of the Fe/Mn/Mg_2-LDH before and after reaction; Figure S5: The N_2 adsorption-desorption isotherm and fitting curve of the BET surface area of the Fe/Mn/Mg_2-LDH before and after reaction; Figure S6: Full XPS spectrum of Fe/Mn/Mg_2-LDH before and after reaction; Figure S7: XPS spectra of C 1s on the Fe/Mn/Mg_2-LDH before and after reaction; Figure S8: Effect of pH and the dosage of Fe/Mn-LDH on the adsorption of Orange II by Fe/Mn-LDH; Figure S9: Effect of pH and the dosage of Fe/Mn/Mg_2-LDH on the adsorption of Orange II by Fe/Mn/Mg_2-LDH; Figure S10: Effect of pH, Fe/Mn/Mg_2-LDH, and PMS concentration on the k_{obs} in the Fe/Mn/Mg_2-LDH/PMS system; Figure S11: Effect of co-existing anions on the k_{obs} in Fe/Mn/Mg_2-LDH/PMS system; Figure S12: Effect of different humic acids on the k_{obs} in Fe/Mn/Mg_2-LDH/PMS system; Figure S13: Catalytic performance of Fe/Mn/Mg_2-LDH in PMS activation for Orange II and TOC removal [51,63–69].

Author Contributions: Conceptualization, Y.W. and P.C.; methodology, Y.W.; validation, C.Q., Y.L. and Y.M.; formal analysis, Y.L.; investigation, C.Q.; resources, Y.W.; data curation, X.T.; writing—original draft preparation, C.Q.; writing—review and editing, Y.W. and P.C.; supervision, P.C. and G.M.; project administration, B.W.; funding acquisition, Y.W. All authors have read and agreed to the published version of the manuscript.

Funding: This research was funded by the National Natural Science Foundation of China, under grant number 21667011, and the Science and Technology Fund of Guizhou Province under grant number ZK[2022]206.

Data Availability Statement: All data discussed in the paper are provided either within the article or in the Supplementary Materials. Raw data files will be provided upon request.

Conflicts of Interest: The authors declare no conflicts of interest.

References

1. Liu, J.; Yang, Q.; Wang, D.; Li, X.; Zhong, Y.; Li, X.; Deng, Y.; Wang, L.; Yi, K.; Zeng, G. Enhanced dewaterability of waste activated sludge by Fe (II)-activated peroxymonosulfate oxidation. *Bioresour. Technol.* **2016**, *206*, 134–140. [CrossRef] [PubMed]
2. Boczkaj, G.; Fernandes, A. Wastewater treatment by means of advanced oxidation processes at basic pH conditions: A review. *Chem. Eng. J.* **2017**, *320*, 608–633. [CrossRef]
3. Yang, Q.; Zhong, Y.; Zhong, H.; Li, X.; Du, W.; Zeng, G. A novel pretreatment process of mature landfill leachate with ultrasonic activated persulfate: Optimization using integrated Taguchi method and response surface methodology. *Process Saf. Environ.* **2015**, *98*, 268–275. [CrossRef]
4. Lee, J.; Von Gunten, U.; Kim, J.H. Persulfate-based advanced oxidation: Critical assessment of opportunities and roadblocks. *Environ. Sci. Technol.* **2020**, *54*, 3064–3081. [CrossRef] [PubMed]
5. Lu, H.; Zou, F.; Liu, X.; Zhang, W.; Zhang, L.; Deng, C.; Yu, Z.; Monfort, O.; Cheng, P. Z-scheme g-C_3N_4/α-FOD heterojunction-assisted persulfate activation for degradation of tetracycline hydrochloride under visible light: Insights into mechanism. *Chem. Eng. J.* **2024**, *479*, 127224. [CrossRef]
6. Gong, C.; Chen, F.; Yang, Q.; Luo, K.; Yao, F.; Wang, S. Heterogeneous activation of peroxymonosulfate by Fe-Co layered doubled hydroxide for efficient catalytic degradation of Rhoadmine B. *Chem. Eng. J.* **2017**, *321*, 222–232. [CrossRef]
7. Rastogi, A.; Al-Abed, S.R.; Dionysiou, D.D. Sulfate radical-based ferrous–peroxymonosulfate oxidative system for PCBs degradation in aqueous and sediment systems. *Appl. Catal. B Environ.* **2009**, *85*, 171–179. [CrossRef]
8. Oh, W.D.; Dong, Z.; Lim, T.T. Generation of sulfate radical through heterogeneous catalysis for organic contaminants removal: Current development, challenges and prospects. *Appl. Catal. B Environ.* **2016**, *194*, 169–201. [CrossRef]
9. Gerken, J.B.; Mcalpin, J.G.; Chen, J.; Rigsby, M.L.; Casey, W.H.; Britt, R.D. Electrochemical water oxidation with cobalt-based electrocatalysts from pH 0–14: The thermodynamic basis for catalyst structure, stability, and activity. *J. Am. Chem. Soc.* **2011**, *133*, 14431–14442. [CrossRef]
10. Anipsitakis, G.P.; Dionysiou, D.D.; Gonzalez, M.A. Radical generation by the interaction of transition metals with common oxidants. *Environ. Sci. Technol.* **2004**, *38*, 3705–3712. [CrossRef]
11. Yang, Q.; Choi, H.; Al-Abed, S.R.; Dionysiou, D.D. Iron–cobalt mixed oxide nanocatalysts: Heterogeneous peroxymonosulfate activation, cobalt leaching, and ferromagnetic properties for environmental applications. *Appl. Catal. B Environ.* **2009**, *88*, 462–469. [CrossRef]
12. Han, B.; Luo, Y.; Lin, Y.; Weng, B.; Xia, D.; Zhou, Y.; Guan, C.; Wang, Z.; Wei, X.; Jiang, J. Microenvironment engineering of single-atom catalysts for persulfate-based advanced oxidation processes. *Chem. Eng. J.* **2022**, *447*, 137551. [CrossRef]
13. Ma, R.; Liu, Z.; Takada, K.; Lyi, N.; Bando, Y.; Sasaki, T. Synthesis and exfoliation of Co^{2+}-Fe^{3+} layered double hydroxides: An innovative topochemical approach. *J. Am. Chem. Soc.* **2007**, *129*, 5257. [CrossRef]
14. Yang, Q.; Zhong, Y.; Li, X.; Xin, L.; Kun, L.; Wu, X.; Chen, H.; Liu, Y.; Zeng, G. Adsorption-coupled reduction of bromate by Fe(II)–Al(III) layered double hydroxide in fixed-bed column: Experimental and breakthrough curves analysis. *J. Ind. Eng. Chem.* **2015**, *28*, 54–59. [CrossRef]
15. Duan, M.; Liu, S.; Jiang, Q.; Guo, X.; Zhang, J.; Xiong, S. Recent progress on preparation and application of layered double hydroxides. *Chin. Chem. Lett.* **2022**, *33*, 4428–4436. [CrossRef]
16. Chen, D.; Yu, Y.; Cheng, P.; Arbid, Y.; Liu, H.; Zou, X.; Chen, T. Utilization of waste adsorbent generated after Ca/Al-LDH adsorption of high-concentration phosphate: Fluorine removal. *J. Environ. Eng. Sci.* **2023**, *149*, 04022090. [CrossRef]
17. Fui, H.; Gao, S.; Ma, X.; Huang, Y. Facile fabrication of CoAl-LDH nanosheets for efficient rhodamine B degradation via peroxymonosulfate activation. *RSC Adv.* **2023**, *13*, 29695–29705. [CrossRef]
18. Huang, X.; Su, M.; Zhou, J.; Shu, W.; Huang, Z.; Gao, N.; Qian, G. Novel activation of persulfate by its intercalation into Mg/Al-layered double hydroxide: Enhancement of non-radical oxidation. *Chem. Eng. J.* **2017**, *328*, 66–73. [CrossRef]
19. Hou, L.; Li, X.; Yang, Q.; Chen, F.; Wang, S.; Ma, Y.; Wu, Y.; Zhu, X.; Huang, X.; Wang, D. Heterogeneous activation of peroxymonosulfate using Mn-Fe layered double hydroxide: Performance and mechanism for organic pollutant degradation. *Sci. Total. Environ.* **2019**, *663*, 453–464. [CrossRef]

20. Zeng, H.; Zhang, W.; Deng, L.; Luo, J.; Zhou, S.; Liu, X.; Pei, Y.; Shi, Z.; Crittenden, J. Degradation of dyes by peroxymonosulfate activated by ternary CoFeNi-layered double hydroxide: Catalytic performance, mechanism and kinetic modeling. *J. Colloid Interface Sci.* **2018**, *515*, 92–100. [CrossRef]
21. Lu, H.; Sui, M.; Yuan, B.; Wang, J.; Lv, Y. Efficient degradation of nitrobenzene by Cu-Co-Fe-LDH catalyzed peroxymonosulfate to produce hydroxyl radicals. *Chem. Eng. J.* **2019**, *357*, 140–149. [CrossRef]
22. Bennekou, P. Cobalt metabolism and toxicology–a brief update. *Sci. Total. Environ.* **2012**, *432*, 210–215.
23. Das, J.; Patra, B.S.; Baliarsingh, N.; Parida, K.M. Adsorption of phosphate by layered double hydroxides in aqueous solutions. *Appl. Clay Sci.* **2006**, *32*, 252–260. [CrossRef]
24. Xu, M.; Pan, G.; Meng, Y.; Guo, Y.; Wu, T.; Chen, H. Effect of Ce^{3+} on the photocatalytic activity of MAlCe ternary hydrotalcites-like compounds in methylene blue photodegradation. *Appl. Clay Sci.* **2019**, *170*, 46–56.
25. Khan, A.A.; Tahir, M.; Khan, N. LDH-based nanomaterials for photocatalytic applications: A comprehensive review on the role of bi/trivalent cations, anions, morphology, defect engineering, memory effect, and heterojunction formation. *J. Energy Chem.* **2023**, *84*, 242–276. [CrossRef]
26. Zhou, H.; Tan, Y.; Yang, Y.; Zhang, Y.; Lei, X.; Yuan, D. Application of FeMgMn layered double hydroxides for phosphate anions adsorptive removal from water. *Appl. Clay. Sci.* **2021**, *200*, 105903. [CrossRef]
27. Magagula, B.; Nhlapo, N.; Focke, W.W. Mn_2Al-LDH and Co_2Al-LDH-stearate as photodegradants for LDPE film. *Polym. Degrad. Stabil.* **2009**, *94*, 947–954. [CrossRef]
28. Velu, S.; Shah, N.; Jyothi, T.M.; Sivasanker, S. Effect of manganese substitution on the physicochemical properties and catalytic toluene oxidation activities of Mg-Al layered double hydroxides. *Microporous Mesoporous Mater.* **1999**, *33*, 61–75. [CrossRef]
29. Gonçalves, R.G.L.; Mendes, H.M.; Bastos, S.L.; D'Agostino, L.C.; Tronto, J.; Pulcinelli, S.H.; Santilli, C.V.; Neto, J.L. Fenton-like degradation of methylene blue using Mg/Fe and MnMg/Fe layered double hydroxides as reusable catalysts. *Appl. Clay Sci.* **2020**, *187*, 105477. [CrossRef]
30. Zhu, J.; Zhu, Z.; Zhang, H.; Lu, H.; Qiu, Y. Efficient degradation of organic pollutants by peroxymonosulfate activated with MgCuFe-layered double hydroxide. *RSC Adv.* **2019**, *9*, 2284. [CrossRef]
31. Chen, G.; Nengzi, L.; Li, B.; Gao, Y.; Zhu, G.; Cheng, X. Octadecylamine degradation through catalytic activation of peroxymonosulfate by Fesingle bondMn layered double hydroxide. *Sci. Total Environ.* **2019**, *695*, 133963. [CrossRef] [PubMed]
32. Ahmadi, M.; Ghanbari, F. Combination of UVC-LEDs and ultrasound for peroxymonosulfate activation to degrade synthetic dye: Influence of promotional and inhibitory agents and application for real wastewater. *Environ. Sci. Pollut. R.* **2018**, *25*, 6003–6014. [CrossRef] [PubMed]
33. Deng, J.; Shao, Y.; Gao, N.; Gao, C.; Zhou, S.; Hu, X. $CoFe_2O_4$ magnetic nanoparticles as a highly active heterogeneous catalyst of oxone for the degradation of diclofenac in water. *J. Hazard. Mater.* **2013**, *262*, 836–844. [CrossRef] [PubMed]
34. Ghanbari, F.; Ahmadi, M.; Gohari, F. Heterogeneous activation of peroxymonosulfate via nanocomposite CeO_2-Fe_3O_4 for organic pollutants removal: The effect of UV and US irradiation and application for real wastewater. *Sep. Purif. Technol.* **2019**, *228*, 115732. [CrossRef]
35. Wang, Y.; Tian, D.; Chu, W.; Li, M.; Lu, X. Nanoscaled magnetic $CuFe_2O_4$ as an activator of peroxymonosulfate for the degradation of antibiotics norfloxacin. *Sep. Purif. Technol.* **2019**, *212*, 536–544. [CrossRef]
36. Ji, Y.; Dong, C.; Kong, D.; Lu, J. New insights into atrazine degradation by cobalt catalyzed peroxymonosulfate oxidation: Kinetics, reaction products and transformation mechanisms. *J. Hazard. Mater.* **2015**, *285*, 491–500. [CrossRef] [PubMed]
37. Deng, J.; Xu, M.; Feng, S.; Qiu, C.; Li, X.; Li, J. Iron-doped ordered mesoporous Co_3O_4 activation of peroxymonosulfate for ciprofloxacin degradation: Performance, mechanism and degradation pathway. *Sci. Total Environ.* **2019**, *658*, 343–356. [CrossRef]
38. Ahmadi, M.; Ghanbari, F.; Alvarez, A.; Martinez, S. UV-LEDs assisted peroxymonosulfate/Fe^{2+} for oxidative removal of carmoisine: The effect of chloride ion. *Korean J. Chem. Eng.* **2017**, *34*, 2154–2161. [CrossRef]
39. Cai, M.; Cheng, P.; Li, J.; Wu, F.; Sarakha, M.; Mailhot, G.; Brigante, M. Toward a better understanding of peroxymonosulfate and peroxydisulfate activation using a nano zero-valent iron catalyst supported on graphitized carbon: Mechanisms and application to the degradation of estorgenic compounds in different water matrix. *J. Clean Prod.* **2023**, *414*, 137702. [CrossRef]
40. Ma, Y.; Chen, F.; Yang, Q.; Zhong, Y.; Shu, X.; Yao, F.; Xie, T.; Li, X.; Wang, D.; Zeng, G. Sulfate radical induced degradation of Methyl Violet azo dye with CuFe layered doubled hydroxide as heterogeneous photoactivator of persulfate. *J. Environ. Manag.* **2018**, *227*, 406–414. [CrossRef]
41. Chen, M.; Huang, Z.; Liang, S.; Pei, F.; Lin, Z.; Dang, Z.; Wu, P. Immobilized Co^{2+} and Cu^{2+} induced structural change of layered double hydroxide for efficient heterogeneous degradation of antibiotic. *J. Hazard. Mater.* **2020**, *403*, 123554. [CrossRef]
42. Chen, F.; Yang, Q.; Li, X.M.; Zeng, G.M.; Wang, D.B.; Niu, C.G.; Zhao, J.W. Hierarchical assembly of graphene-bridged Ag_3PO_4/Ag/$BiVO_4$ (040) Z-scheme photocatalyst: An efficient, sustainable and heterogeneous catalyst with enhanced visible-light photoactivity towards tetracycline degradation under visible light irradiation. *Appl. Catal. B Environ.* **2017**, *200*, 330–342. [CrossRef]
43. Zhu, B.; Zhao, H.; Kalyanaraman, B.; Frei, B. Metal independent production of hydroxyl radicals by halogenated quinones and hydrogen peroxide: An ESR spin trapping study. *Free Radic. Bio. Med.* **2002**, *32*, 465e473. [CrossRef]
44. Chen, F.; Yang, Q.; Zhong, Y.; An, H.; Zhao, J.; Xie, T. Photo-reduction of bromate in drinking water by metallic Ag and reduced graphene oxide (RGO) jointly modified $BiVO_4$ under visible light irradiation. *Water Res.* **2016**, *101*, 555–563. [CrossRef] [PubMed]

45. Weng, Z.; Lin, Y.; Guo, S.; Zhang, X.; Guo, Q.; Luo, Y.; Ou, X.; Ma, J.; Zhou, Y.; Jiang, J.; et al. Site engineering of covalent organic frameworks for regulating peroxymonosulfate activation to generate singlet oxygen with 100 % selectivity. *Angew. Chem. Int. Ed. Engl.* **2023**, *62*, e202310934. [CrossRef]
46. Wu, D.; Zong, Y.; Tian, Z.; Shao, B. Role of reactive oxygen species in As (III) oxidation by carbonate structural Fe (II): A surface-mediated pathway. *Chem. Eng. J* **2019**, *368*, 980–987. [CrossRef]
47. Yang, S.; Xiao, T.; Zhang, J.; Chen, Y.; Li, L. Activated carbon fiber as heterogeneous catalyst of peroxymonosulfate activation for efficient degradation of Acid Orange 7 in aqueous solution. *Sep. Purif. Technol.* **2015**, *143*, 19–26. [CrossRef]
48. Zhang, X.; Wang, Y.; Li, G.; Qu, J. Oxidative decomposition of azo dye CI Acid Orange 7 (AO7) under microwave electrodeless lamp irradiation in the presence of H_2O_2. *J. Hazard. Mater.* **2006**, *134*, 183–189. [CrossRef]
49. Chen, D.; Ma, X.; Zhou, J.; Chen, X.; Qian, G. Sulfate radical-induced degradation of Acid Orange 7 by a new magnetic composite catalyzed peroxymonosulfate oxidation process. *J. Hazard. Mater.* **2014**, *279*, 476–484. [CrossRef]
50. Ji, C.; Xu, M.; Yu, H.; Lv, L.; Zhang, W. Mechanistic insight into selective adsorption and easy regeneration of carboxyl-functionalized MOFs towards heavy metals. *J. Hazard. Mater.* **2022**, *424*, 127684. [CrossRef]
51. Huang, G.; Wang, C.; Yang, C.; Guo, P.; Yu, H. Degradation of bisphenol A by peroxymonosulfate catalytically activated with $Mn_{1.8}Fe_{1.2}O_4$ nanospheres: Synergism between Mn and Fe. *Environ. Sci. Technol.* **2017**, *51*, 12611–12618. [CrossRef]
52. Yang, B.; Tian, Z.; Wang, B.; Sun, Z.; Zhang, L.; Guo, Y.; Li, H.; Yan, S. Facile synthesis of Fe_3O_4/hierarchical-Mn_3O_4/graphene oxide as a synergistic catalyst for activation of peroxymonosulfate for degradation of organic pollutants. *RSC Adv.* **2015**, *5*, 20674–20683. [CrossRef]
53. Fan, J.; Qin, H.; Jiang, S. Mn-doped g-C_3N_4 composite to activate peroxymonosulfate for acetaminophen degradation: The role of superoxide anion and singlet oxygen. *Chem. Eng. J.* **2019**, *359*, 723–732. [CrossRef]
54. Huang, J.; Zhang, H. Mn-based catalysts for sulfate radical-based advanced oxidation processes: A review. *Environ. Int.* **2019**, *133*, 105141. [CrossRef]
55. Zhao, X.; Niu, C.; Zhang, L.; Guo, H.; Wen, X.; Liang, C.; Zeng, G. Co-Mn layered double hydroxide as an effective heterogeneous catalyst for degradation of organic dyes by activation of peroxymonosulfate. *Chemosphere* **2018**, *204*, 11–21. [CrossRef]
56. Wang, Y.; Sun, H.; Ang, H.M. 3D-hierarchically structured MnO_2 for catalytic oxidation of phenol solutions by activation of peroxymonosulfate: Structure dependence and mechanism. *Appl. Catal. B Environ.* **2015**, *164*, 159–167. [CrossRef]
57. Liu, X.; Yuan, B.L.; Zou, J.; Wu, L.B.; Dai, L.; Ma, H.F.; Li, K.; Ma, J. Cu(II)-enhanced degradation of acid orange 7 by Fe(II)-activated persulfate with hydroxylamine over a wide pH range. *Chemosphere* **2019**, *238*, 124533. [CrossRef]
58. Luo, S.; Wei, Z.; Dionysiou, D.D.; Spinney, R.; Hu, W.P.; Chai, L.; Yang, Z.; Ye, T.; Xiao, R. Mechanistic insight into reactivity of sulfate radical with aromatic contaminants through single-electron transfer pathway. *Chem. Eng. J.* **2017**, *327*, 1056–1065. [CrossRef]
59. Zhou, H.; Jiang, Z.; Wei, S. A new hydrotalcite-like absorbent FeMnMg-LDH and its adsorption capacity for Pb^{2+} ions in water. *Appl. Clay. Sci.* **2018**, *153*, 29–37. [CrossRef]
60. Lou, X.; Guo, Y.; Xiao, D.; Wang, Z.; Lu, S.; Liu, J. Rapid dye degradation with reactive oxidants generated by chloride-induced peroxymonosulfate activation. *Environ. Sci. Pollut. R.* **2013**, *20*, 6317–6323. [CrossRef] [PubMed]
61. Viollier, E.; Inglett, P.W.; Hunter, K.; Roychoudhury, A.N.; Van Cappellen, P. The Ferrozine method revisted. *Appl. Geochem.* **2000**, *15*, 785–790. [CrossRef]
62. Pan, T.; Wang, Y.; Yang, X.; Huang, X.F.; Qiu, R. Gallic acid accelerated BDE47 degradation in PMS/Fe (III) system: Oxidation intermediates autocatalyzed redox cycling of iron. *Chem. Eng. J.* **2020**, *384*, 123248. [CrossRef]
63. Lu, H.; Zhu, Z.; Zhang, H.; Zhu, J.; Qiu, Y. Simultaneous removal of arsenate and antimonate in simulated and practical water samples by adsorption onto Zn/Fe layered double hydroxide. *Chem. Eng. J.* **2015**, *276*, 365–375. [CrossRef]
64. Xie, L.; Zhong, Y.; Xiang, R.; Fu, G.; Xu, Y.; Cheng, Y. Sono-assisted preparation of Fe(II)-Al(III) layered double hydroxides and their application for removing uranium (VI). *Chem. Eng. J.* **2017**, *328*, 574–584. [CrossRef]
65. Zhou, Y.; Jiang, J.; Gao, Y.; Ma, J.; Pang, S.; Li, J.; Lu, X.; Yuan, L. Activation of Peroxymonosulfate by Benzoquinone: A Novel Nonradical Oxidation Process. *Environ. Sci. Technol.* **2015**, *49*, 12491–12950. [CrossRef]
66. Ding, Y.; Xia, X.; Ruan, Y.; Tang, H. In situ H+-mediated formation of singlet oxygen from BaBiO3 for oxidative degradation of bisphenol A without light irradiation: Efficiency, kinetics, and mechanism. *Chemosphere* **2015**, *141*, 80–86. [CrossRef]
67. Fang, G.; Dionysiou, D.D.; Al-Abed, S.R.; Zhou, D. Superoxide radical driving the activation of persulfate by magnetite nanoparticles: Implications for the degradation of PCBs. *Appl. Catal. B* **2013**, *129*, 325–332. [CrossRef]
68. Zhang, J.; Shao, X.; Shi, C.; Yang, S. Decolorization of Acid Orange 7 with peroxymonosulfate oxidation catalyzed by granular activated carbon. *Chem. Eng. J.* **2013**, *232*, 259–265. [CrossRef]
69. Yang, B.; Liu, H.; Zhang, J. High-valent metals in advanced oxidation processes: A critical review of their identification methods, formation mechanisms, and reactivity performance. *Chem. Eng. J.* **2023**, *460*, 141796. [CrossRef]